Journal of Power Sources 653 (2025) 237784

Contents lists available at ScienceDirect

Journal of Power Sources

journal homepage: www.elsevier.com/locate/jpowsour

Highly active and stable Fe-N_4 catalyst from unused natural resources for oxygen reduction reaction in acidic to alkaline medium

Edwin Osebe Nyangau [a], Hiroya Abe [b], Kazutoshi Haga [c], Chie Ooka [a], Kenji Hayashida [d], Naoka Nagamura [e,f], Kotaro Takeyasu [g], Masaru Watanabe [a], Yuta Nakayasu [a,b,*]

[a] Research Center of Supercritical Fluid Technology, Graduate School of Engineering Tohoku University, 6-6-11, Aoba, Aza, Aramaki, Aoba-ku, Sendai, Miyagi, 980-8579, Japan
[b] Frontier Research Institute for Interdisciplinary Sciences, Tohoku University, 6-3, Aramaki-aza Aoba, Aoba-ku, Sendai, 980-8578, Japan
[c] Graduate School of International Resource Science, Akita University, 1-1 Tegatagakuen-machi, Akita, 010-8502, Japan
[d] Graduate School of Science and Technology, University of Tsukuba, 1-1-1 Tennodai, Tsukuba, Ibaraki, 305-8573, Japan
[e] Center for Basic Research on Materials, National Institute for Materials Science, 3-13 Sakura, Tsukuba, Ibaraki, 305-0003, Japan
[f] Graduate School of Advanced Engineering, Tokyo University of Science, 6-3-1, Niijuku, Katsushika, Tokyo, 125-8585, Japan
[g] Institute for Catalysis, Hokkaido University, N21W10, Sapporo, Hokkaido, 001-0021, Japan

HIGHLIGHTS

- Fe–N_4 site stabilization gives 17 % higher stability than Pt/C in acidic media.
- Catalyst synthesized from rice husks and mining waste for ORR applications.
- Unique fifth coordination forms between Fe–N_4 and amorphous SiO_2 from rice husks.
- Delivers 160 mW cm^{-2} in Zn–air batteries, outperforming Pt/C at 120 mW cm^{-2}.

GRAPHICAL ABSTRACT

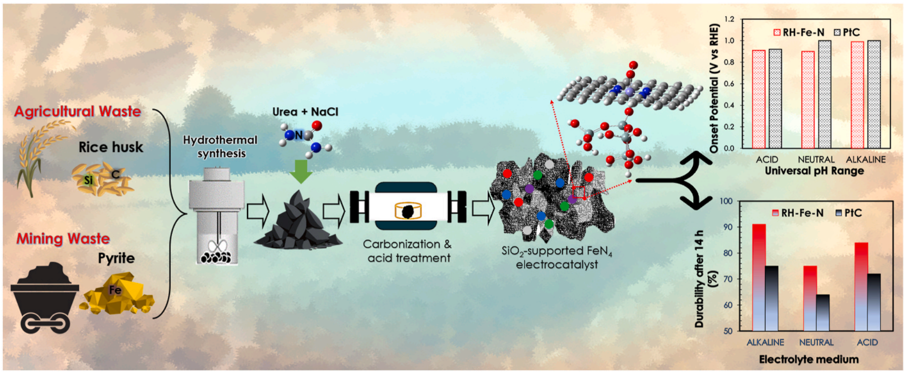

ARTICLE INFO

Keywords:
Fe-N_4
Oxygen reduction reaction
Catalyst stability
Universal pH
Fe-N-C

ABSTRACT

Iron–nitrogen–carbon (Fe–N–C) catalysts with Fe–N_4 coordination are promising alternatives to platinum-based materials for the oxygen reduction reaction (ORR), yet their instability in acidic media limits practical applications. Herein, we report a sustainable Fe–N–C catalyst (RH-Fe-N) synthesized from rice husks and pyrite, serving as carbon and iron sources, respectively. This approach eliminates the need for complex precursors such as metal–organic frameworks, using a simple three-step carbonization method including hydrothermal carbonization. The resulting catalyst incorporates Fe atoms into a carbon matrix with self-doped amorphous SiO_2 from rice husks. Spectroscopic and theoretical analysis reveals a unique fifth Fe–O coordination within the SiO_2 matrix, enhancing site stability and ORR activity. In Zn–air battery applications, RH-Fe-N achieves a peak power

---

* Corresponding author. Frontier Research Institute for Interdisciplinary Sciences, Tohoku University, 6-3, Aoba, Aza, Aramaki, Aoba-ku, Sendai, Miyagi, 980-8578, Japan.

E-mail address: yuta.nakayasu.b6@tohoku.ac.jp (Y. Nakayasu).

https://doi.org/10.1016/j.jpowsour.2025.237784
Received 31 January 2025; Received in revised form 16 May 2025; Accepted 25 June 2025
Available online 30 June 2025

density of 160 mW cm^{-2}, outperforming commercial Pt/C (40 wt%) at 120 mW cm^{-2}, with a higher open-circuit voltage (1.50 V vs. 1.40 V for Pt/C). The catalyst also demonstrates superior durability, with 17 % and 16 % higher stability than Pt/C in acidic and neutral conditions, respectively. This work provides a low-cost, scalable, and eco-friendly strategy for developing high-performance ORR catalysts across all pH ranges, contributing to sustainable energy generation and circular economy goals.

1. Introduction

The interplay of agricultural practices, renewable energy technologies and waste management reveals key areas where innovative solutions can mitigate environmental impacts. On the agricultural aspects, the production of staple foods like rice, consumed by over half the global population, generates approximately 150 million tons of rice husks (RH) annually [1]. Due to their high silica content and low nitrogen levels, RH resists decomposition, limiting its use as a composite fertilizer [2]. To manage these wastes quickly, farmers often burn RH in kilns, but this action has been found to be associated with releasing harmful fine particle pollutants which contribute to greenhouse gas emissions [3]. These challenges highlight the urgent need for sustainable RH recycling solutions to mitigate environmental impacts [4].

The rising demand for copper, driven by the proliferation of electric vehicles (EVs), has led to increased extraction of its primary source, chalcopyrite. This process generates significant amounts of pyrite (FeS_2) as waste [5]. However, pyrite is often discarded in landfills during mining operations, and its effective utilization from industrial sources remains underdeveloped. Pyrite, composed of 53.5 % sulfur and 44.9 % iron, contributes to substantial mining waste [6]. When exposed to groundwater, it can undergo chemical reactions that result in highly acidic soils and water systems, causing severe harm to ecosystems [7–9]. These environmental issues highlight the urgent need for improved waste management practices and the development of value-added processes to mitigate the ecological impact of mining operations.

In the past many researchers have reported numerous works focused on enhancing biomass wastes by developing raw materials for batteries, capacitors, or supercapacitors entirely or partially derived from biomass wastes [10–15].The outstanding feature of most of these works has been the significance of heteroatom doping onto the biomass-derived carbon. Nitrogen functionalities and iron have been particularly successful in this regard. Specifically, doping biomass-derived carbon with pyridinic N and graphitic N has been shown to improve oxygen (O_2) adsorption on neighboring carbon atoms [16–18]. In addition, the metal heteroatoms of metal-nitrogen macrocyclic compounds ($M - N_4$) act as efficient and robust oxygen reduction reaction (ORR) active sites [19–22]. This enhancement facilitated the desired $4e^-$ transfer pathway during the ORR [23–26].

Over the past decade, researchers have highlighted that while Fe-N-C catalysts exhibit high ORR activity as an alternative to platinum in proton exchange membrane fuel cells (PEMFC), their limited stability remains a barrier to commercialization [27]. To enhance stability, efforts have focused on modifying catalyst structure, morphology, and chemistry by optimizing synthesis parameters such as heat treatment, atmospheric conditions, and precursor compositions [28–32]. One widely reported approach to address the low stability in Fe-N-C has been through multiple heteroatom doping, particularly with metallic elements like titanium (Ti). Titanium has been reported to improve Fe-N-C stability by strengthening the bond between Fe and nitrogen thus preventing the leaching of the Fe active sites [33]. Similarly, the selectivity of the type of nitrogen dopant has weighed in on the catalyst performance and stability. For instance, graphitic and pyridinic N are associated with higher ORR activity and stability due to lower overpotentials and increased charge density at the active sites [25,34–37].

Despite the above-mentioned modification of the Fe-N-C catalyst showing better stability and high ORR activities, their application has only been limited to alkaline medium applications pausing a challenge in universal pH medium applications. This has been attributed to the fact that these catalysts are more stable and durable in alkaline conditions compared to other media such as a neutral or acidic medium [38–42]. Low stability in an acidic medium for instance has been linked to the excessive demetallation of the Fe species and carbon corrosion at high potentials hence reducing the active site density and resulting in low catalyst stability [30–43].

One promising approach to improving stability across all pH ranges is through the optimization of the catalyst's coordination environment. Studies have shown that FeN_4 sites with pyrrolic nitrogen are more prone to Fe leaching than those with pyridinic nitrogen, suggesting that the local electronic environment around Fe plays a critical role in minimizing leaching and improving stability [44]. By fine-tuning the coordination of nitrogen dopants around the central Fe atom, particularly through heteroatom doping, it is possible to improve the catalyst's durability and performance in both acidic and alkaline media. Such modifications may also enhance protonation states, further stabilizing the Fe-N-C active sites during electrochemical reactions.

In this study, we present a novel tri-doped, biomass-derived electrocatalyst tailored for advanced electrochemical energy storage systems, particularly in diverse battery environments. Derived from agricultural waste (rice husks) rich in silica and mining by-products (pyrite) containing iron, these abundant and typically polluting materials are transformed through a sustainable, multi-step synthesis involving low-temperature hydrothermal carbonization and template-assisted pyrolysis. This process yields a highly porous carbon matrix enhanced by nanoreactor formation and pyrolysis gases during template carbonization, optimizing the catalyst's structure and surface chemistry.

The resulting Si/Fe/N tri-doped carbon electrocatalyst demonstrates exceptional ORR activity and durability across a universal pH range; alkaline, neutral, and acidic surpassing conventional biomass-derived and Fe–N–C catalysts. The synergistic interaction between $Fe–N_4$ active sites and amorphous SiO_2 contributed to enhanced active site stability and prolonged catalytic performance. Unlike conventional Fe–N–C catalysts that rely solely on nitrogen coordination, this tri-doped system leverages the synergistic effects of SiO_2 and $Fe-N_4$ to provide a more stable and efficient catalyst.

Due to its high performance, environmental sustainability, and cost-effectiveness, this catalyst is well-suited for a wide range of battery technologies, including metal air battery in alkaline environment, microbial fuel cells in neutral medium and proton-exchange membrane fuel cells in acidic environment, offering a promising pathway toward durable, green energy storage solutions operable in diverse electrolyte environments.

2. Experimental section

2.1. Catalyst synthesis

Locally sourced pyrite was first crushed using a jaw crusher (P-1, Fritsch Japan Co, Ltd) and a disc mill (P-13, Fritsch Co, Ltd). The obtained ore was classified as −75 μm as the experiment feed using a vibratory sieve shaker (A-3, Fritsch Co, Ltd). Coarse particles remaining on the sieve were pulverized again using a vibrating cup mill (P-9, Fritsch Japan Co, Ltd). 20 g of the finely ground pyrite powder was then mixed with 200 ml of distilled water and introduced into a 500 ml stainless steel autoclave (Toyo Kouatsu). 1 MPa of pure oxygen was then purged severally into the autoclave before subjecting the autoclave to

170 °C for 1 h. After allowing the reactor to cool down to room temperature, the mixture slurry was filtered through filter paper (Advantech Toyo, Japan). The collected solution was then analyzed using an inductively coupled plasma mass spectroscopy (ICP-MS) to quantify the concentration of the elements in the filtrate solution.

100 ml of the obtained pyrite solution was then mixed with 5 g of evenly crushed RH (Ogata, Akita-Japan) of an average diameter of 150 μm–250 μm in a 500 ml batch-type autoclave reactor (Taiatsu, Japan). 200 ml of distilled water was then added and the reactor was purged with Nitrogen gas severally to create an inert atmosphere in the reactor. After this, the pressure inside was adjusted by injecting nitrogen gas until 2 MPa was achieved. The reactor was then subjected to 250 °C for 6 h. The self-generated pressure inside the reactor rose to a constant 5 MPa for the entire duration of 6 h as continuous stirring at 300 rpm was maintained. After the set time lapsed the reactor was cooled down to room temperature and the pre-carbonized RH slurry was then vacuum filtered through a 5.0 μm type 2 filter paper (Advantech Toyo, Japan), and the residue solids were collected and dried at 105 °C overnight.

The dried hydrochar was then mixed with NaCl and Urea in a 1:3:8 mass ratio. The mixture was then ground manually into a homogenous mixture using a ceramic mortar and pestle. The mixture was then loaded onto an alumina crucible and subjected to template carbonization using NaCl as a precursor. The mixture was heated in a tubular furnace at 750 °C at a ramp rate of 5 °C/min. The heating was then kept constant for 2 h and the temperature was allowed to cool to room temperature. The carbonized char was then collected and refluxed using 3M HCl overnight to remove any unreacted NaCl. After filtration, the solids were washed severally using distilled water until a pH of 7 was obtained and the collected char was dried again at 105 °C.

The dried char was then finally carbonized at 850 °C for 1 h and the final RH-derived catalyst doped with Fe and N was collected and labeled as RH-Fe-N. As a control to this catalyst, pristine rice husk with neither pyrite nor urea was synthesized in the same conditions and labeled as Pristine RH in this work. To systematically investigate the influence of structural and compositional parameters on catalytic performance, a series of control samples were synthesized. Catalysts subjected to different pyrolysis temperatures were labeled RHN@750 °C and RHN@950 °C, enabling assessment of how thermal treatment affects the development of active sites and overall electrocatalytic activity. In addition, to evaluate the specific role of amorphous SiO_2, another control was prepared by selectively etching silica from the rice husk precursor using KOH, as described in the Supplementary Information. This approach facilitated the isolation of the SiO_2 contribution to the stabilization of Fe–N_4 active sites and the resulting catalytic effects. The collected catalysts were then characterized as detailed below.

2.2. Physiochemical characterization

Ultra-high resolution imaging field emission scanning electron microscope (FE-SEM S-4800, Hitachi, Japan) coupled with the element energy-dispersive X-ray spectrometer (EMAX-EDS) were used to characterize the synthesized catalysts apparent morphology and the surface element distribution with an operation voltage of 5–15 kV. The magnification varied between 1K and 200K. The corresponding TEM characterization was achieved by using a transmission electron microscope (TEM, HT-7500, Hitachi Ltd) with an operation voltage of 100–200 kV, and composition was analyzed using (TEM-EDS, JEM-2100F, JEOL). The catalyst solution was introduced dropwise onto TEM grids with carbon support (JEOL, Japan) and allowed to dry at room temperature before analysis.

The crystal structure of the synthesized electrocatalysts was analyzed by $\theta-2\theta$ horizontal multi-purpose X-ray diffraction (XRD; Ultiman IV RIGAKU, Japan) with Cu-Kα radiation ($\lambda = 1.5406$ Å), a tube voltage of 40 kV and tube current 40 mA at a step size of 0.05° and a scan rate of 2 $\min^{-1}$. A measurement range of between $10^\circ-80^\circ$ was analyzed. An integrated PDXL software (RIGAKU) was then used for qualitative analysis of the peaks. A laser Raman microscope (Raman Force, Japan) with 532 nm excitation wavelength, 2000 cm^{-1} central wavenumber, × 20 objective and a 30-s exposure time was used for spectra acquisition. The obtained spectra were analyzed using Raman imager 2. The chemical states of the electrocatalysts were analyzed by X-ray photoelectron spectroscopy (XPS; PHI 5000 Versa Probe I) using an A1 Kα source to characterize the elemental and bonding states. For qualitative analysis of the individual N 1s and Fe 2p contents, a MULTIPAK spectrum software was used (ULVAC-PHI).

Atomic analyses on the coordination environment of the synthesized electrocatalyst were achieved using the Fe K-edge and Si-K-edge X-ray absorption near edge structure (XANES) and extended X-ray absorption fine structure (EXAFS). This was achieved using an XAFS (Hard X-ray) I BLS51 beamline with an energy range of 5–22 kV (Aichi SR, Japan) for the Fe K-edge. The Si-K-edge was achieved using XAFS (Soft X-ray) BL6N1 beamline with a DSP ROI of 1605–1875 eV (Aichi SR, Japan) The synthesized catalyst was measured and mixed with boron nitrate and the mixture used to make tablets as per the XAFS sample preparation guide (SPring-8 BL14B2 public). The acquired EXAFS data was processed according to standard procedures using the ATHENA module implemented in the IFEFFIT software package. The EXAFS spectra were obtained by subtracting the post-edge background from the overall absorption and normalizing with respect to the edge-jump step. Subsequently, the χ(k) data were Fourier transformed into real (R) space using a Hanning window (dk = 1.0 $Å^{-1}$) to isolate EXAFS contributions from different coordination shells.

To extract quantitative structural parameters around the central Fe atom, the least-squares curve-fitting was performed using the ARTEMIS module of the IFEFFIT software suite, based on the following EXAFS equation:

$$\chi(\mathrm{k}) = S_0{}^2 \sum_j \frac{N_j\, F_j\,(k) \exp\left(-2k^2 \sigma_j{}^2\right)}{kR_j{}^2} \sin\left(2kR_j + \varnothing_j(k)\right)$$

Where $S_0{}^2$ is the amplitude reduction factor, $F_j\,(k)$ is the effective curved-wave backscattering amplitude, N_j is the coordination number in the j-th shell,r_j is the absorber backscattered distance, $\varnothing_j$ is the total phase shift, and $\sigma_j{}^2$ is the Debye-Waller factor representing disorder. The fitting model for Fe K-edge was constructed using a monoclinic Fe_2NO_8 crystal structure from a CIF file as a theoretical reference. This structure included a known local coordination geometry where the Fe atom is bonded to four nitrogen atoms (degeneracy = 4) and a single axial oxygen atom (degeneracy = 1). Initially, the coordination numbers were fixed according to this known degeneracy. The amplitude reduction factor $S_0{}^2$ was refined to 0.941 ± 0.076 and then fixed in subsequent fits. The structural parameters bond distances R_j, Debye-Waller factors $\sigma_j{}^2$ and edge-energy shift ΔE_0 were allowed to float. Similarly, Si K-edge EXAFS fitting was achieved by incorporating scattering paths derived from the $FeSiO_3$ crystal structure as a theoretical reference with $S_0{}^2$ refined at 0.787 then fixed subsequently.

2.3. Electrochemical measurements and battery evaluation

The synthesized catalyst materials were characterized using a rotating ring disk electrode (RRDE-3A, BAS, Japan) equipped with a bi-potentiostat (ALS/DY 2325, BAS, Japan). Electrochemical characterization was made possible using a three-electrode cell consisting of an Ag/AgCl reference electrode, Pt counter wire electrode, and the RRDE as the working electrode. To prepare the working electrode for the electrochemical analysis, 4 mg of the synthesized catalyst was dispersed in a solvent containing 6 μL Nafion® solution (527,084, Sigma Aldrich, USA), 334 μL distilled water, and 84 μL isopropyl alcohol. The mixture was then subjected to ultra-sonication in a sonic bath (Branson) for 3 min 15 μL of the resulting ink solution was then introduced onto the polished glassy carbon (GC, BAS Co. Ltd., Japan). The GC was then allowed to dry at room temperature. In this work, 0.1M KOH pH 13, 0.1 M PB solution pH 7.2, and 0.1 M H_2SO_4 pH 1 were used as ORR electrolyte medium after bubbling with either N_2 or O_2 gas for about 20 min. As a comparison, a similar ink as outlined above was synthesized but using 3 mg of the synthesized catalyst and 1 mg of Denka carbon black. Subsequent steps for ink formation and GC preparation remained the same as outlined above.

In both electrolyte media, LSV was obtained at a scan rate of 10 mVs^{-1} and a rotation speed of 1600 rpm. In neutral conditions, a potential range of 0.5 V to −0.5 V vs. Ag/AgCl was investigated, in acidic conditions, a potential range of 1.1 V to −1 V vs. Ag/AgCl while a potential range of 0.2 V to −0.8 V vs. Ag/AgCl was monitored in an alkaline medium. The potential of the ring electrode was set to 1.2V, 0.8V, and 0.8 V vs. Ag/AgCl constant for acidic, neutral, and alkaline medium. Cyclic voltammetry (CV) was also evaluated at a scan rate of 50 mV/s in both conditions with continuous O_2 or N_2 gas bubbling. Other electrochemical measurements carried out in this work include durability, Methanol, and potassium cyanide (KCN) stability as per previously reported works of literature. As a control, the electrochemical analysis described above was conducted using a 40 wt% commercial

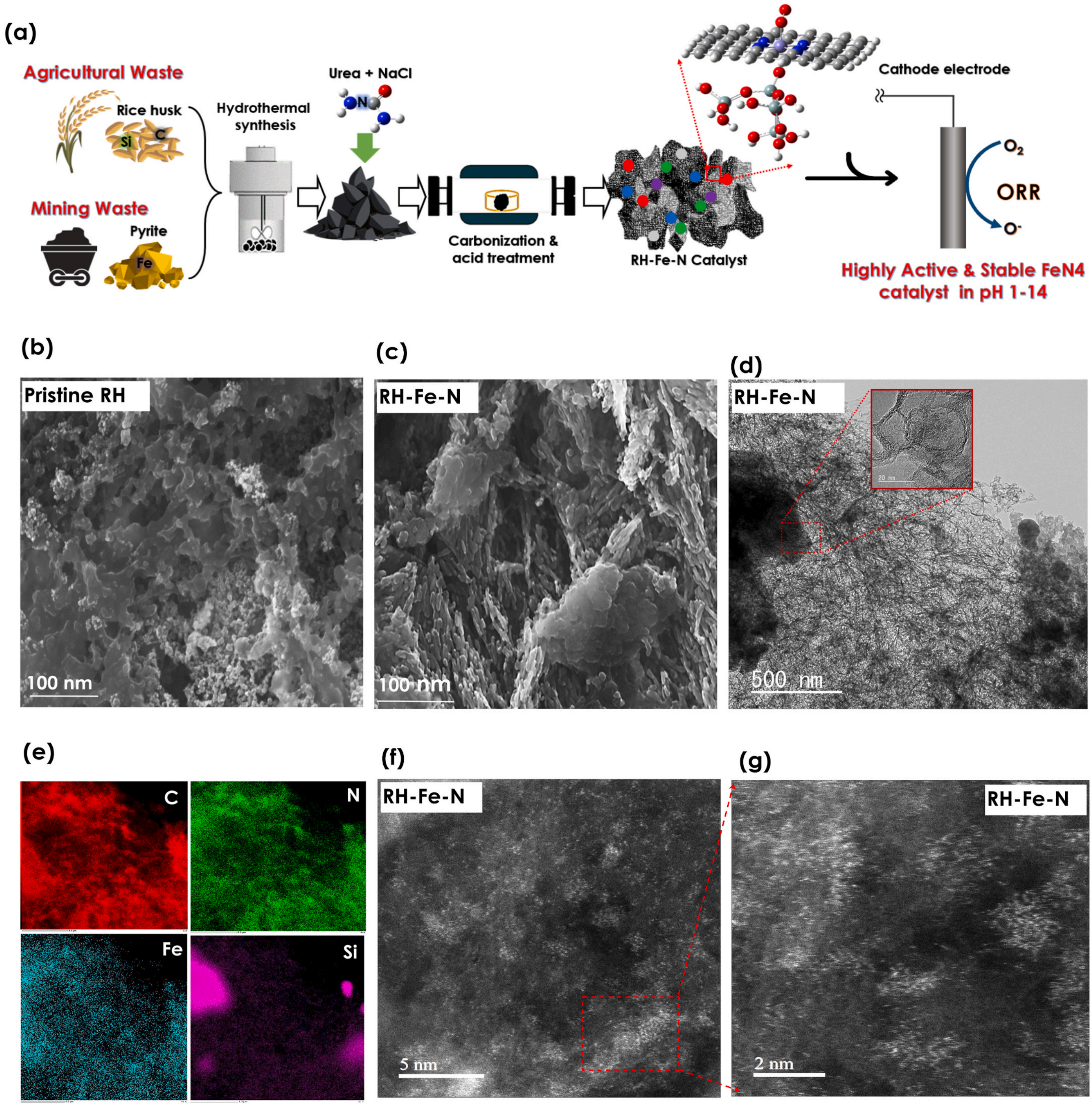

Fig. 1. Catalyst synthesis and morphology characterization. (a) Schematics of RH-Fe-N catalysts synthesis. Scanning electron microscopy images (SEM) for (b) Pristine RH and (c) RH-Fe-N. High resolution Transmission Electron Microscopy (TEM) images of (d) RH-Fe-N and their corresponding (e) EDS mapping after template carbonization. (f) HAADF-STEM image of RH-Fe-N, showing Fe atomic distribution on the RH derived carbon and (g) higher magnification of cluster like regions.

platinum catalyst.

To assess the practical application of the prepared catalysts, a ZAB was assembled. The anode consisted of polished zinc foil with a thickness of 0.5 mm. The electrolyte was a mixed aqueous solution of 6 M KOH and 0.2 M $Zn(CH_3COO)_2$. The air cathode was fabricated by uniformly applying RH-Fe-N-CB catalyst ink onto conductive carbon paper (gas diffusion layer) with a loading of 1 mg cm^{-2}. For comparison, 40 wt % Pt/C was used as the control electrocatalyst. Discharge polarization curves were recorded at a scan rate of 5 mVs^{-1} using an Ivium potentiostat, with additional battery analyses performed according to previously reported methods.

2.4. Density functional theory (DFT) computational details

The extent and role of amorphous silica in stabilizing the Fe-N_4 moiety was characterized by DFT calculations using the Gaussian 16 software package with the B3LYP hybrid functional along with 6-31G(d, p) basis sets for C, N, and H, and lanl2dz for Fe and Si [35,45–47]. All initial structures before optimization with DFT were generated by GaussView6.1 with the initial distance between the Fe atom and the (Fe-O) ligand fixed between 1.97 and 2.0 Å as per the XAS analysis outcome.

3. Results and discussion

The synthesis of RH-Fe-N was achieved through a multistage carbonization process, consisting of three main steps: (1) pre-carbonization with iron doping, (2) simultaneous carbonization and activation via template carbonization, and (3) acid treatment followed by nitrogen annealing as illustrated in Fig. 1a. The first step involved hydrothermal carbonization of precursor materials, specifically pyrite and RH. During this process, iron (Fe) was incorporated into the RH-derived hydrochar, forming iron-doped carbon precursors. Subsequently, a simultaneous activation and carbonization process was employed to further modify the material using a sacrificial template carbonization conducted at 750 °C in the presence of NaCl and urea.

In this step, NaCl served as a template to achieve porosity in the RH carbon structure, while the addition of urea aided in the formation of nitrogen-containing functionalities. After templating carbonization, the resulting biochar material underwent acid treatment and neutralization to remove any residual salts and impurities. Finally, the activated precursor was subjected to nitrogen annealing at 850 °C resulting in the formation of the final product labeled as RH-Fe-N in this work. The as prepared catalysts were then subjected to various characterizations as discussed in the subsequent sections.

3.1. Synthesis and morphology of the catalyst

Pyrite was subjected to oxidative dissolution using a low-temperature hydrothermal process (170 °C for 1 h) in an oxygenated medium, resulting in an oxidized pyrite solution. This solution was rich in SO_4^{2-} and Fe^{2+} ions, as confirmed by inductively coupled plasma mass spectrometry (ICP-MS) analysis *(*Fig. S1*)*. The high SO_4^{2-} concentration in the solution was responsible for the low pH recorded in the pyrite solution, which is a known condition that enhance the solubility of iron precursors during hydrothermal carbonization processes [48]. This was crucial in the subsequent stage of hydrothermal carbonization in this work, where the pyrite solution was mixed with RH and subjected to 250 °C for 6 h. The combination of low pH and elevated temperature further increased the concentration of Fe^{2+} ions, promoting stronger interactions between the RH carbon matrix and iron [49]. These conditions facilitated efficient Fe doping onto the RH carbon matrix as confirmed by various physicochemical characterization outlined in subsequent sections.

As shown in the SEM images in Fig. 1(b and c), despite both Pristine RH and RH-Fe-N being subjected to the same carbonization temperatures, the effect of sacrificial template carbonization using NaCl and urea was clear in RH-Fe-N. This sample exhibited a more pronounced 3D, rugged, and irregular morphology, as depicted in Fig. 1c, in contrast to the more compact and poorly developed porous structure observed in Pristine RH (Fig. 1b**)**. The transition to a looser, more porous structure in RH-Fe-N was primarily driven by the interaction between the carbon substrate and pyrolysis gases, such as NH_3, which were generated from urea during N_2 annealing within the confined nanoreactors created by NaCl crystals. This process facilitated the formation of numerous micropores and mesopores, underscoring the critical role of NaCl and urea in promoting porosity during synthesis process [50–52].

In addition, this gasification effect of NH_3 within the enclosed nanoreactor resulted in N atoms incorporation in the RH carbon matrix and hence trapping the already pre-doped Fe atoms in the microporous sites [53]. The resulting RH-Fe-N morphology, with its enhanced porosity, is expected to improve exposure of active sites and facilitate efficient mass transport during ORR activity. The extent of porosity and heteroatom dispersion within the microporous structure of the RH-Fe-N carbon matrix was further investigated using TEM analysis. Unlike the generally compact and dense morphology exhibited by RH-Fe-N before template carbonization as shown in Fig. S2, the RH-Fe-N TEM image after template carbonization displayed a homogeneous, wrinkled surface morphology across the observable area, with a wide region covered by transparent regions as shown in Fig. 1d**.**

This indicated the formation of porosity in RH-Fe-N after template carbonization, consistent with the earlier SEM observations. A high-resolution TEM image of RH-Fe-N, shown in Fig. 1d (inset), revealed numerous highly ordered mesoporous structures with an average mesopore diameter of approximately 20 nm. These mesopores provided edge sites that facilitated the immobilization of the doped heteroatoms. This was further confirmed by energy dispersive X-ray spectroscopy (EDS) mapping as shown in Fig. 1e. The EDS analysis detected the presence of C, N, and Fe that were homogeneously dispersed along the mesopores. Although the EDS mapping revealed a general dispersion of Si throughout the observed region, there were some segregations of the Si as depicted by the silica-rich clusters.

Furthermore, bamboo-like carbon nanotube (CNT) structures were observed in the TEM images Fig. 1d which are characteristic of iron-catalyzed growth during the carbonization process. To investigate the nature and distribution of iron species responsible for this morphology, aberration-corrected high-angle annular dark-field scanning transmission electron microscopy (HAADF-STEM) was performed on the RH-Fe-N catalysts, as shown in Fig. 1e and f. At the 5 nm scale (Fig. 1f), numerous isolated bright spots were detected, uniformly distributed across the field of view. These features were consistent with atomically dispersed Fe species, as further supported by EDS mapping (Fig. 1e). Additionally, a few localized regions (highlighted by red rectangles) suggested the presence of small crystalline iron oxide nanoclusters, although these were sparse and scattered.

To further analyze these regions, higher magnification HAADF-STEM images (2 nm scale, Fig. 1g) were acquired. These confirmed that atomically dispersed Fe remains the predominant species, with only minor fuzzy aggregates likely corresponding to ultra-small Fe oxide clusters. The chemical nature of these Fe species was further examined using X-ray photoelectron spectroscopy (XPS), X-ray absorption spectroscopy (XAS), and X-ray diffraction (XRD), as detailed in subsequent sections. These analyses confirmed the successful incorporation of Fe and N as heteroatoms into the RH-derived carbon matrix, along with self-doped SiO_2 from the precursor material (RH).

Similarly, the overlapping elemental distribution of Fe and N in EDS mapping suggests a strong interaction between these elements, likely leading to the formation of Fe–N_4 moieties, which act as active sites for ORR activities [22,53]. Additionally, this uniform and homogeneous distribution of doped elements was expected to significantly enhance the catalyst's stability during the ORR process [54,55]. To understand the nature and type of porosity achieved in the RH-Fe-N catalyst, Brunauer-Emmett-Teller (BET) analysis and density functional theory (DFT) adsorption-desorption isotherms were conducted as shown in Fig. S3. A distinct nitrogen adsorption at relatively low relative pressures in the RH-Fe-N catalyst compared to Pristine RH, confirmed the presence of micropores in the RH-Fe-N catalyst as revealed by BET.

The nature and type of micropores formed in RH-Fe-N as investigated using DFT, revealed a hierarchical porous structure with two main pore diameters in the ranges of 0.4–0.5 nm and 0.6–0.8 nm, with most of the pores cantered in the 0.6–0.8 nm range. On the other hand, Pristine RH exhibited only one type of micropore, mainly centered between 0.5 and 0.6 nm. These average pore diameters in the RH-Fe-N catalyst were sufficiently large to accommodate most of the hydrated ions found in ORR electrolyte solutions, such as K^+ (diameter 0.66 nm), Na^+ (diameter 0.72 nm), Cl^- (diameter 0.66 nm), PO_4^{3-} (diameter 0.67 nm) and OH^- (diameter 0.6 nm) [56,57]. This was essential in facilitating the mass transport of these ions to the active sites immobilized within the micropores, thereby enhancing the electrolytic kinetics of the catalyst. This phenomenon was further confirmed by the higher ORR activity observed in the RH-Fe-N catalyst compared to Pristine RH, as discussed in the subsequent section.

3.2. Activity and stability for ORR

The influence of the doped heteroatoms (Si, Fe, and N) in promoting ORR activity was investigated using a rotating ring disk electrode (RRDE) in 0.1 M KOH, 0.1 M PB, and 0.1 M H_2SO_4 solutions. This was achieved using a linear sweep voltammetry (LSV) at a scan rate of 10 mVs^{-1} and 1600 rpm in both N_2 and O_2 saturated electrolyte solutions. All potentials were referenced to the reversible hydrogen electrode (RHE). The LSV curves shown here represent the difference between the LSVs in O_2-saturated electrolytes and those in N_2-saturated electrolytes. As shown in Fig. 2a, in 0.1 M KOH solution, the onset potentials (E_{onset}) defined as at 0.01 $mAcm^{-2}$ were 0.99 V for RH-Fe-N, and 1.00 V for commercial 40 wt% PtC and 0.76 V for Pristine RH. This exceptional onset potential exhibited by RH-Fe-N was consistent with the corresponding half-wave potential ($E_{1/2}$) of 0.80, 0.84, and 0.65 V for RH-Fe-N, PtC, and Pristine RH respectively. RH-Fe-N ORR activities far exceeded those of pristine RH and almost equaled those of commercial PtC. This superior ORR activity was owing to the well-developed hierarchical pore structure and the homogenous dispersion of doped heteroatoms in the micropore and mesopores in RH-Fe-N as earlier presented under the morphology characterization section.

The excellent ORR activity of the RH-Fe-N catalyst, compared to commercial Pt/C in an alkaline medium, was also replicated in near-neutral conditions. With an onset potential of 0.90 V compared to 1.00 V achieved by commercial Pt/C under 0.1M PB as shown in Fig. 2b, the RH-Fe-N catalyst demonstrated promising performance. Although this value was generally lower than that of Pt/C, the RH-Fe-N activity still ranked among the highest reported in near-neutral media, as recently documented by Vo T. et al. [58]. The well-developed hierarchical morphology, along with the edge defects discussed earlier in the morphology characterization, contributed to the exposure of active sites within the RH-Fe-N catalyst, thus enhancing its ORR activity. Additionally, the exceptional onset potential in RH-Fe-N was accompanied by a superior half-wave potential of 0.73 V, slightly below that of commercial Pt/C at 0.78 V.

When the ORR activities were analyzed under acidic conditions (0.1 M H_2SO_4), a similar trend to that observed in alkaline and neutral media was recorded. RH-Fe-N achieved a remarkably high onset potential of 0.91 V, compared to 0.92 V for 40 wt% Pt/C, as shown in Fig. 2c. The

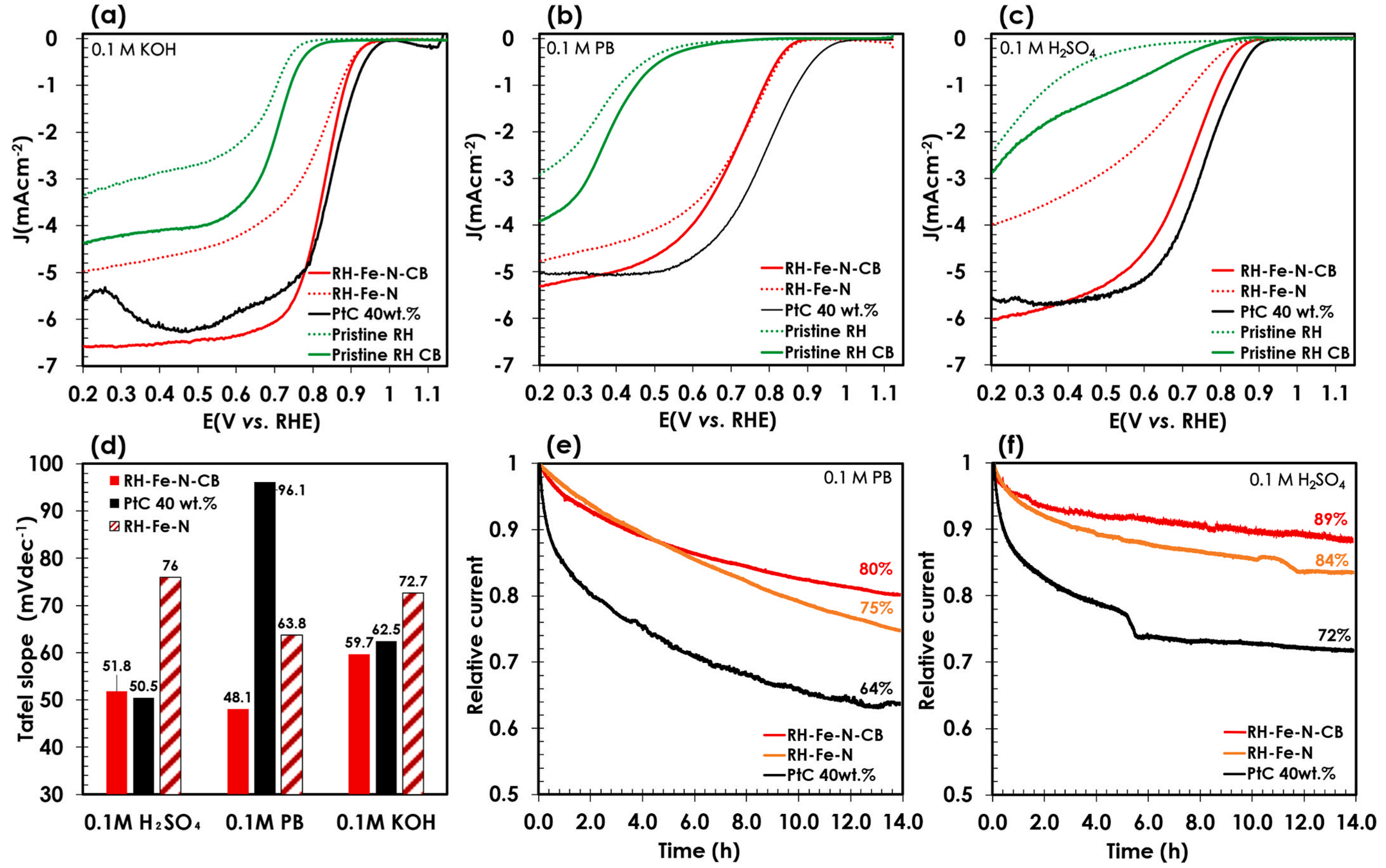

Fig. 2. Electrochemical performance of as prepared catalysts. LSV curves of the as prepared catalysts under (a) 0.1M KOH, (b) 0.1M PB and (c) 0.1M H_2SO_4. (d) Tafel slopes of as prepared catalyst in 0.1M KOH, 0.1M PB and 0.1M H_2SO_4. Normalized current vs time curves for RH-Fe-N vs commercial 40 % PtC measured at 0.8V and at 1600 rpm in saturated and (e) 0.1M PB (f) 0.1M H_2SO_4.

high activity in the acidic medium could be attributed to the improved dispersion of Fe and N within the micropores of RH-Fe-N, in addition to the enhanced stability provided by the self-doped amorphous SiO_2, which helped limit the dissolution of the active Fe-N_4 sites [59]. However, despite this high onset potential in an acidic medium, a concern arose due to the low current density, even at large overpotentials. This was particularly evident as the current density was lower than the diffusion-limited current density at 0.2 V vs RHE. As previously reported by Santosh K.et al., this phenomenon was hypothesized to be due to the low diffusion of protons (H^+) in the diffusion region during ORR [60].

To address this issue, we added commercial carbon black to the prepared catalysts at a ratio of 1:4 and repeated the ORR analysis. Samples containing the commercial carbon black were labeled with the acronym "CB". Intriguingly, the onset potentials of RH-Fe-N-CB and Pristine RH-CB across all media remained relatively unchanged; however, there was a significant increase in the current densities. This effect was especially pronounced in alkaline and acidic media, as depicted in Fig. 2a and (c) respectively. The increased current densities for both RH-Fe-N-CB and Pristine RH-CB in the diffusion region of the LSV plot confirmed that the addition of conductive carbon black improved the diffusion of oxygen ions and protons [60].

To further understand the superior ORR activities exhibited by RH-Fe-N before and after the addition of conductive carbon black, Tafel slopes were measured and compared with those of commercial Pt/C, as shown in Fig. 2d for alkaline, neutral, and acidic media. Surprisingly, RH-Fe-N-CB exhibited a superior Tafel slope compared to commercial Pt/C across all media. The faster ORR kinetics, as confirmed by a superior Tafel slope of 59.7 $mV\cdot dec^{-1}$ (compared to 62.5 $mV\cdot dec^{-1}$ for 40 wt% Pt/C in alkaline medium, were responsible for the high ORR activities discussed earlier. This was further accompanied by an average electron transfer number of 3.9, compared to 4 for Pt/C, as shown in Fig. S4. This demonstrated that RH-Fe-N followed the desirable 4-electron transfer pathway during the ORR process, with an average hydrogen peroxide (H_2O_2) yield below 5 %, compared to 2 % for 40 wt% Pt/C.

The trend in Tafel slope and electron transfer number observed between RH-Fe-N-CB and Pt/C was consistent across all media, including lower pH conditions. RH-Fe-N-CB demonstrated an even lower Tafel slope of 51.8 $mV\cdot dec^{-1}$ in acidic medium while commercial Pt/C achieved 50.5 $mV\cdot dec^{-1}$ in the same medium. This further confirmed the even faster ORR kinetics in RH-Fe-N-CB as confirmed by a nearly perfect 4-electron transfer pathway, with an extremely low H_2O_2 yield averaging 1.52 %, which was comparable to that of commercial Pt/C. The number of electron transfer were further confirmed using a Nabae model as shown in Fig. S5 which exhibited almost 75 % of ORR reactions taking place in the 4-electron region.

Overall, RH-Fe-N exhibited exceptional performance across all universal pH media, nearly matching the ORR activities of state-of-the-art commercial Pt/C. As discussed earlier, the high activity was attributed to the well-developed hierarchical porosity and the homogeneous dispersion of heteroatoms within the micropores. However, the application of Fe-N-C-based catalysts has been limited to alkaline environments due to the poor stability of such catalysts under neutral and acidic conditions. Motivated by the excellent catalytic performance of RH-Fe-N under neutral and acidic conditions, this study further investigated its stability and durability, especially in low pH environments; conditions in which traditional Fe-N-C catalysts typically exhibit low long-term performance due to degradation of the Fe related active sites.

After 14 h of continuous operation in 0.1 M H_2SO_4 at a constant voltage of 0.8 V and 1600 rpm, RH-Fe-N-CB retained 89.0 % of its initial current, outperforming RH-Fe-N (84.0 %) and the commercial Pt/C catalyst (72.0 %), as shown in Fig. 2f. This exceptional stability under acidic conditions is indicative of superior resistance to active site degradation, a common challenge for Fe-N-C catalysts [30,43]. In contrast, under neutral conditions, RH-Fe-N-CB also demonstrated remarkable durability, maintaining 80 % of its initial current, representing a 25 % improvement over the Pt/C catalyst (Fig. 2e). This result highlighted the catalyst's superior performance in both acidic and neutral environments suggesting its potential for practical applications in wide ranges of pH media.

The enhanced long-term stability of RH-Fe-N catalysts was attributed to the improved dispersion and embedding of doped elements such as Si, Fe, and N within the carbon matrix. These dopants not only stabilized the active sites, preventing their erosion but also facilitated faster interfacial charge transfer, which was crucial for maintaining high catalytic activity even under prolonged operation [59].

To further understand the role of amorphous SiO_2 in stabilizing Fe–N_4 sites, a selective etching experiment was conducted using concentrated KOH to remove SiO_2 from the RH precursor, as detailed in the Supporting Information. XRD analysis of the KOH-treated RH precursor (Fig. S8a) confirmed the partial removal of the SiO_2 phase, while the graphitic carbon structure remained intact. This proved that the etching process effectively targeted the silica without compromising the overall carbon framework. Following this step, the catalyst synthesis was completed using the KOH-etched precursor, and the resulting material was evaluated for ORR activity.

A significant shift in ORR performance marked by a $\Delta E_{1/2}$ of 85 mV was observed between RH-Fe-N and the catalyst derived from the KOH-treated precursor (Fig. S8b). This notable decline in performance underscores the crucial role of amorphous SiO_2 in enhancing ORR activity, likely through stabilization of Fe–N_4 moieties and modification of their local electronic structure. These findings were further clarified by X-ray absorption spectroscopy (XAS) and theoretical density functional theory (DFT) calculations, which are discussed in the subsequent sections.

To isolate the individual contributions of NaCl and urea during the catalyst's synthesis, various control samples were prepared by omitting either NaCl or urea under identical conditions. The resulting catalysts, RH-Fe-N (without NaCl) and RH-Fe-N (without urea) were benchmarked against the fully synthesized RH-Fe-N-CB and the Pristine RH (without either additive), as shown in (Fig. S9). Linear sweep voltammetry using RRDE revealed that RH-Fe-N-CB exhibited a superior onset potential of 0.98 V vs. RHE, outperforming RH-Fe-N without NaCl (0.878V) and RH-Fe-N without urea (0.84 V), confirming the synergistic contribution of NaCl (a porosity inducer) and urea (as a nitrogen source and porosity inducer) in enhancing ORR activity.

To further optimize the synthesis, the carbonization temperature was varied between 750 °C and 950 °C. There was an obvious increase in ORR activities as the synthesis temperature increased from 750 °C to 850 °C but when the temperature increased to 950 °C there was a drastic drop in onset potential as shown in(Figure S9b). Further clarification on this phenomenon was confirmed using DFT-based adsorption–desorption isotherms as shown in (Figure S3c). The DFT-based adsorption–desorption isotherms showed that RH-Fe-N prepared at 850 °C developed a hierarchical microporous structure with dominant pore sizes between 0.4–0.5 nm and 0.6–0.8 nm which were sufficiently large to enable efficient ion transport of hydrated K^+, Na^+, Cl^-, PO_4^{3-}, and OH^- ions during ORR analysis. In contrast, samples treated at 950 °C exhibited pore collapse due to structural sintering whose effects were evident from the diminished ORR activity (Figure S9b). Pristine RH, with its narrow and poorly distributed pores, lacked this hierarchical porosity, leading to the lowest ORR performance. These results demonstrated the critical role of both NaCl and urea, as well as the importance of optimal carbonization temperature (850 °C), in achieving highly active and stable ORR catalysts.

3.3. Identification of Fe-N_4 active sites

To understand the exceptional ORR activity of RH-Fe-N, several physicochemical characterizations were conducted and compared with various reference samples, including Pristine RH as a negative control. Powder X-ray diffraction (XRD) analysis, shown in Figure S10, was used to confirm the successful doping of heteroatoms in the synthesized electrocatalysts. RH-Fe-N exhibited a distinct peak at 22.0°, attributed to amorphous SiO_2 from the self-doped silica in RH. Similarly, RH-Fe-N sample exhibited multiple minor iron peaks between 43° and 50° mainly indexed to Fe_3C. These findings confirmed the successful recovery of Fe from pyrite and its incorporation into biomass-derived carbon during the hydrothermal process.

To seek clarity on the nature and type of interaction between these heteroatom dopants, X-ray photoelectron spectroscopy (XPS) analysis was carried out on the as prepared catalysts. A high-resolution XPS survey scan revealed four distinct groups of sharp peaks in both pristine RH and RH-Fe-N, as shown in Figure.S11. Peaks observed between 100 and 200 eV in binding energy were attributed to Si (Si 2p), with the dominant peak between 280 and 290 eV corresponding to C (C 1s). A peak around 526–536 eV was attributed to O (O 1s), indicating the presence of oxygen in the carbon matrix. Notably, a clear N1s peak at approximately 400 eV was detected in RH-Fe-N, while a poorly resolved N 1s peak was observed in pristine RH, confirming successful nitrogen doping into the RH carbon structure via urea addition during the template carbonization process.

Similarly, traces of Fe 2p peak was detected around 720 eV on the RH-Fe-N spectrum while the same could not be detected on the pristine RH spectrum. Intriguingly, despite the high content of sulfur (S) in the pyrite solution used as an Fe dopant, no significant S doping was achieved in the RH-Fe-N catalyst as shown from the RH-Fe-N XPS survey. This was further, clarified using CHNSO elemental analysis on the synthesized RH-Fe-N ash samples. The CHNSO analysis results, as shown in Figure.S12, revealed that the sulfur content in both samples was very low, with only trace amounts of sulfur ($\leq 0.07\%$) incorporated into the carbon matrix during synthesis. This suggests that although the oxidized pyrite solutions contain a significant amount of SO_4^{2-}, the sulfur species did not substantially doped into the final carbon structure. This was attributed to the minimal sulfur incorporation to the nature of the synthesis conditions, where the high-temperature treatment under inert atmosphere likely prevented significant sulfur retention.

The high-resolution N 1s spectrum was deconvoluted into three distinct peaks located at 398.3, 399.4, and 401.2 eV, corresponding to pyridinic-N, pyrrolic-N, and graphitic-N, respectively as shown in Fig. 3a. The higher concentration of electron-donating pyridinic-N and electron-conducting graphitic-N in RH-Fe-N suggested that the catalyst possessed enhanced electrocatalytic properties [61], which likely contributed to its superior ORR activity compared to pristine RH. Pyrrolic-N, which is known to promote a 2-electron transfer pathway during ORR [36], was detected at low atomic concentration in RH-Fe-N. This, along with the higher concentrations of pyridinic-N and graphitic-N, supported the catalyst's preference for a more efficient 4-electron transfer pathway across all pH media as earlier discussed.

The high-resolution Fe 2p XPS spectrum, shown in Fig. 3b, revealed two distinct peaks (Fe $2p_3/_2$ at around and Fe $2p_1/_2$) in RH-Fe-N, which were absent in pristine RH. The deconvoluted Fe 2p XPS spectrum featured Fe^{2+} $2p_{3/2}$ at approximately 710.5 eV and Fe^{3+} $2p_{3/2}$ at around 713.7 eV, along with their corresponding $2p_{1/2}$ peaks at 723.8 eV and 727.1 eV respectively. In addition, characteristic satellite peaks were detected at approximately 716.3 eV and 730.5 eV. Consequently, no distinct peak corresponding to metallic Fe^0 (typically observed near 706.6 eV) was detected. This affirmed that Fe doped into the RH-Fe-N catalyst existed in oxidized form with mixed oxidation states or coordinated forms rather than in its elemental state. This observation aligned well with the XRD, HAADF and TEM results, confirming the successful recovery and doping of Fe from the pyrite solution. The existence of multiple oxidation states of Fe pointed at high degree of atomic interaction between Fe and N in RH-Fe-N. Such interactions are believed to have played a crucial role in the formation of $Fe\text{-}N_4$ active sites, which were associated with enhanced catalytic activity [62].

To investigate the effect of Fe loading on catalytic performance, RH-Fe-N samples were synthesized using different RH-to-pyrite molar ratios (1:5 and 1:10), along with a control sample without pyrite. XPS analysis of the Fe 2p spectra *(*Figure.S13a*)* revealed that higher pyrite content (1:5 ratio) led to stronger Fe^{2+}/Fe^{3+} signals, indicating more effective

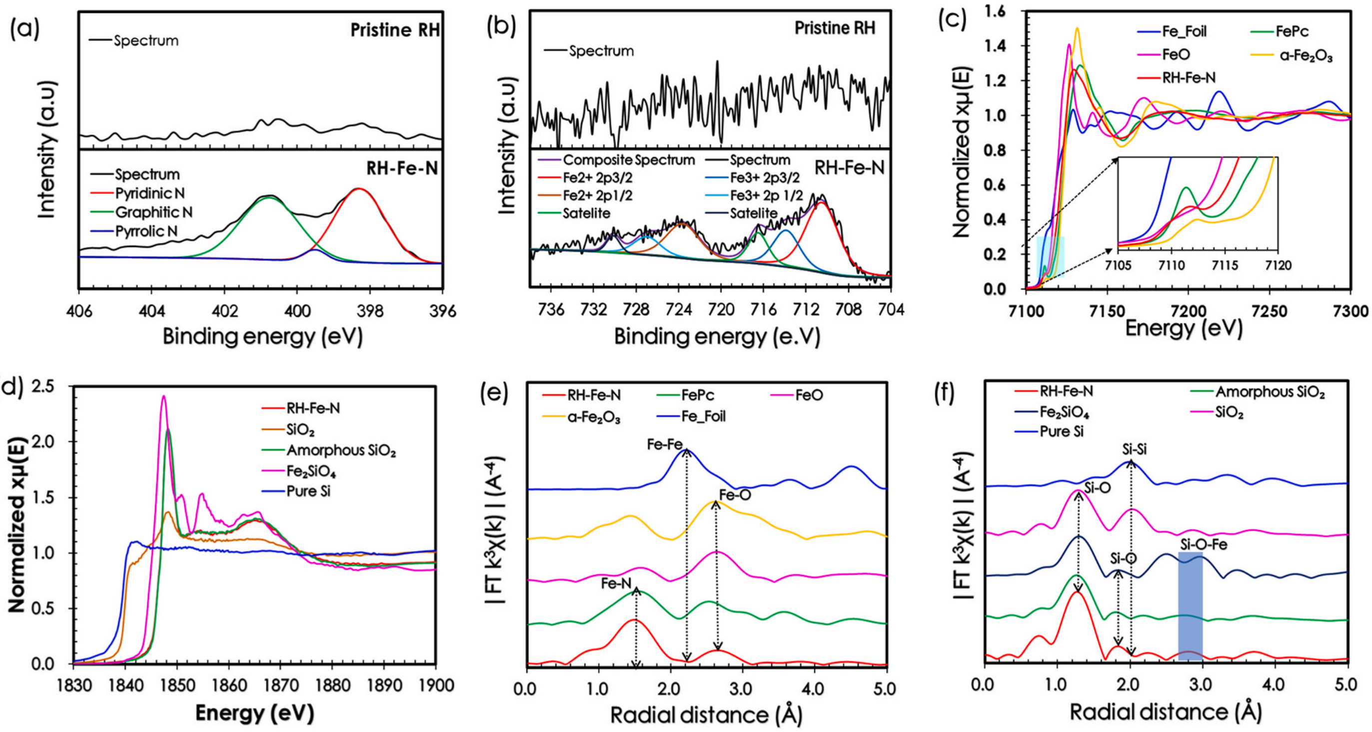

Fig. 3. Identification of Fe-N-C active sites. (a) High resolution N 1s analysis for as prepared RH-Fe-N as compared to that of Pristine RH catalyst and (b) a corresponding high resolution Fe 2p survey. (c)Fe K-edge XANES spectrum of RH-Fe-N together with various reference compounds for comparison. (d) Si K-edge XANES spectrum of RH-Fe-N together with various reference compounds for comparison and their corresponding FT-EXAFs relating to (e) Fe K-edge FT-EXAFS of as prepared RH-Fe-N catalyst compared with various standard references. (f) Si K-edge FT-EXAFS of as prepared RH-Fe-N catalyst compared with various standard references.

incorporation of iron into the carbon matrix. In contrast, the 1:10 sample showed weaker Fe signals, while the pyrite-free control exhibited no detectable iron. This trend confirmed that pyrite was the primary Fe source in the RH-Fe-N catalyst.

These variations impact on the ORR performance were analyzed as shown Figure.S13b. The RH-Fe-N 1:5 catalyst demonstrated the highest ORR activity, attributed to optimal formation of Fe–N_x active sites. Lower activity in the 1:10 and pyrite-free samples correlated with reduced iron content and fewer active sites. In line with the aim of this work on sustainability, the 1:5 RH-to-pyrite molar ratios were considered for this work and higher loading ratios were disregarded at this time. These findings highlight the critical role of pyrite concentration in tuning Fe incorporation and optimizing electrocatalytic activity in RH-derived carbon catalysts.

To clarify the chemical state, electronic structure, and interactions of doped heteroatoms in RH-Fe-N, X-ray absorption spectroscopy (XAS) was performed and compared with standard references. The Fe K-edge XANES spectra of RH-Fe-N was traced between the peaks of FeO (Fe^{2+}) and α-Fe_2O_3 (Fe^{3+}) spectra suggesting the co-existence of Fe^{2+}/Fe^{3+} oxidation states. This was consistent with other spectroscopy analysis such as XPS and other material analyses such as TEM, HAADF and XRD that hinted at the existence of surface Fe oxides on the RH-Fe-N catalyst. A detailed inspection of the pre-edge region (7105 eV–7120 eV) revealed an almost similar pre-edge shoulder peak to those of FePc and α-Fe_2O_3 though smaller in intensity compared to FePc but larger than α-Fe_2O_3 around 7111 eV.

To clearly distinguish the adjacent elements with nearby atomic numbers such as Fe-N, Fe-O and other bonds, an analysis of the Fourier-transformed (FT) EXAFS region of RH-Fe-N was carried out, as shown in Fig. 3e. RH-Fe-N exhibited a broad peak at approximately 1.59 Å which was in line with the Fe-N scattering path in FePc. This confirmed a possible 4 Fe-N coordination environment which is attributed to the formation of porphyrin-like configurations (Fe-N_4). Such structures are commonly associated with active sites during ORR [22,34]. Furthermore, a distinct peak at approximately 2.60 Å corresponding to the Fe-O scattering path was observed, indicating the co-existence of Fe with surface oxide species. Interestingly, no significant Fe-Fe scattering path was detected at 2.20 Å, which implied that the Fe atoms were atomically dispersed rather than clustered and were likely bonded with other elements such as N, C or linked with amorphous SiO_2. This finding was consistent with both HAADF, TEM and XPS analyses, further confirming the atomic dispersion of Fe in the RH carbon matrix hence creating active sites in the mesopores and micropores. The nature of coordination was confirmed by fitting the experimental data on Artemis software as discussed in subsequent section.

The structure and coordination of self-doped silica on RH-derived carbon were also characterized using soft X-ray absorption spectroscopy (XAS). A Si K-edge XANES spectra of RH-Fe-N revealed an almost perfect alignment with both amorphous SiO_2 as shown in Fig. 3d. This observation was further supported by the Si-K-edge Fourier transform (FT) spectra as shown in Fig. 3f, which displayed a Si-O peak at approximately 1.3 Å, a feature common to almost all references investigated besides those of pure Si. A distinct shoulder peak was detected around 1.8–1.9 Å. This peak, which is presumed to correspond to a second Si–O coordination, resembles those observed in the Fe_2SiO_4 reference and amorphous SiO_2, but was not present in the SiO reference. This unique feature suggests the possibility of coordination between Si and other elements via a silica oxide linkage. These observations indicated that RH-Fe-N contained a mixture of silica phases, likely amorphous, and potentially involving other oxide linkages. Further analysis of the RH-Fe-N EXAFS data in the 2–4 Å region revealed peaks resembling those found in amorphous SiO_2, including a distinct feature near 2.9 Å corresponding to the shoulder peak of Fe_2SiO_4. This suggested the possible formation of Si–O–Fe linkages. These results support the hypothesis of the presence of amorphous silica within the RH-Fe-N catalyst and possible coordination with Fe. In mixed-valence Fe^{2+}/Fe^{3+} systems such as amorphous silicate glasses, a possible reduction in the average Si oxidation state to approximately +2.5–3.0 may lead to a more acute Si–Fe bond angle and thus a shorter bond length [63].

Similarly, in RH-Fe-N sample, where amorphous SiO_2 is believed to axially coordinate to the FeN_4 site, the Si K-edge EXAFS spectrum exhibited a second-shell peak at approximately 2.8 Å. This slightly shorter Si–Fe distance suggests an even more bent Si–Fe geometry, potentially reflecting a highly distorted interfacial linkage between the Fe center and the silica matrix. The observed deviation from literature values may indicate a lower local coordination symmetry or a more electron-rich environment, further supporting the formation of structurally integrated Si–O–Fe linkages at the FeN_4 site. The nature of this coordination was further examined through fitting the experimental Si K-Edge data on Artemis software as discussed in subsequent section. Notably, the absence of a distinct Si peak in RH-Fe-N indicated that silica was chemically bonded to other elements, which suggested possible formation of edge defects on the carbon lattice that could serve as active sites for ORR activities.

The hypothesized presence of Fe-N_4 active sites in RH-Fe-N, were confirmed experimentally by introducing potassium cyanide (KCN) into a 0.1 M KOH electrolyte during linear sweep voltammetry (LSV) analysis. Cyanide ions (CN^-) are known to compete with O_2 for active sites in Fe-N_4 sites [64], as such the addition of KCN was expected to significantly reduce the ORR activity of a catalyst containing Fe-N_4 sites. This claim was confirmed as shown in Figure.S14, the onset potential of RH-Fe-N dropped by almost 153 mV after KCN was added. However, when KCN was washed off from the electrode with water and the electrolyte was replaced with only 0.1 M KOH, there was a notable recovery in the onset potential. This indicates that CN^- temporarily blocked the Fe-N_4 sites in the RH-Fe-N catalyst [35]. After washing away the cyanide, the catalyst restored its initial ORR performance, confirming that the Fe-N_4 active sites were still present and functional. These results corroborate the presence of Fe-N_4 sites as suggested by the XAS analysis hence explaining the superior ORR activities exhibited by RH-Fe-N across all pH media.

3.4. *Stabilization of Fe-N_4 active sites by SiO_2*

As outlined in preceding sections, the superior catalytic activity of RH-Fe-N catalysts across a wide range of pH conditions can be attributed to the excellent and uniform distribution of doped heteroatoms, including self-doped amorphous SiO_2. As discussed earlier, the interactions between these dopants and the RH carbon matrix result in multiple coordination modes at the active sites. One of the key modes is the postulated four-fold coordination (Fe-N_4) between iron (Fe) and nitrogen (N) besides the possibility of a fifth coordination between Fe and surface oxides functional groups as indicated by earlier XPS and XAFS analyses. To clarify this hypothesis, both experimental analysis via Artemis fitting of experimental data and theoretically using density functional theory (DFT) calculations were carried out as detailed below.

The acquired experimental EXAFS data was processed according to standard procedures using the ATHENA module implemented in the IFEFFIT software package [65].The EXAFS spectra were obtained by subtracting the post-edge background from the overall absorption and normalizing with respect to the edge-jump step. Subsequently, the χ(k) data were Fourier transformed into real (R) space using a Hanning window ($dk = 1.0\ \text{Å}^{-1}$) to isolate EXAFS contributions from different coordination shells. To extract quantitative structural parameters around the central atom for both Fe K-Edge and Si K-Edge, the least-squares curve-fitting was performed using the ARTEMIS module of the IFEFFIT software suite.

For Fe K-Edge fitting, a model was constructed using a monoclinic Fe_2NO_8 crystal structure (ICSD ID:87421) as a theoretical reference. This structure included a known local coordination geometry where the Fe atom is bonded to four nitrogen atoms (degeneracy = 4) and a single axial oxygen atom (degeneracy = 1). Initially, the coordination numbers were fixed according to this known degeneracy. The amplitude reduction factor S_0^2 was refined to 0.941 ± 0.076 and then fixed in subsequent fits. The structural parameters bond distances R_j, Debye-Waller factors $\sigma_j{}^2$ and edge-energy shift ΔE_0 were allowed to float. The fitted EXAFS spectrum is as shown in Fig. 4a and a detailed summary of the fitting parameters is provided in Table S1. This quantitative EXAFS fitting confirmed a Fe-N_4 coordination in the first scattering path shell, with a refined coordination number (CN) of around 4, bond length R(Å) of 1.97 Å, and Debye-Waller factor $\sigma_j{}^2 = 0.01023$. The EXAFS analysis revealed a primary Fe-N_4 coordination environment, with a fitted Fe-N bond length of 1.97 Å, corresponding to a Fourier-transformed (FT) EXAFS peak at around 1.59 Å(Fig. 3e). This peak, after accounting for a phase shift, aligns with the fitted Fe-N bond length and hence consistent with porphyrin-like Fe-N_4 structures, such as iron phthalocyanine (FePc). A secondary, weaker scattering path, attributed to an axial Fe-O interaction (interpreted as a fifth ligand), was observed at a fitted distance of 3.06 ± 0.02 Å, with coordination number (CN) of around 1.00 and $\sigma_j{}^2 = 0.00792$. This corresponded to the FT-EXAFS peak at around 2.60 Å after accounting for phase shifts during fitting. The Fe-N and Fe-O scattering paths were well-fitted to the RH-Fe-N data at the Fe K-edge, with a reduced chi-square of 29.49 and an R-factor of 0.0073, indicating high fitting quality. These results collectively confirm the presence of a Fe-N_4 moiety with a potential axial oxygen ligand, underscoring the role of Fe and N heteroatoms in the enhanced ORR activity of the RH-Fe-N catalyst across a universal pH range

Similarly, Si K-edge EXAFS fitting incorporating scattering paths derived from the $FeSiO_3$ crystal structure (ICSD ID: 75928) was demonstrated. In this case, not only first shell scattering but also longer-range Si–Fe paths were aimed to examine the possibility of Si–O–Fe bonding in the RH-Fe-N catalyst. The fitted Si K-Edge EXAFS spectrum is as shown in Fig. 4b and a detailed summary of the fitting parameters is provided in Table S2. This quantitative EXAFS fitting provided more insights, especially on the shoulder peak observed near 1.8 Å in the Fourier-transformed EXAFS spectrum. This peak was well accounted for by a second-shell O scatterer (Si-O) at R about 1.64 Å with a refined coordination number (CN) of 2.00, bond length R(Å) of 1.64 Å, and Debye-Waller factor $\sigma_j{}^2 = 0.0035$. Moreover, a longer-range scattering path at around 3.09 Å with a refined coordination number (CN) of 1.00, bond length R(Å) of 3.087 Å and Debye-Waller factor $\sigma_j{}^2 = 0.0056$ was identified and assigned to a Si–O–Fe interaction. This distance was consistent with a Fe-O shell identified on the Fe-K-edge fit at 3.06 ± 0.02 Å. This path supports the hypothesis at a possible O ligand bridging Si and Fe atoms, which was consistent with the features observed in both of the experimental EXAFS spectrum for Fe-K-edge(Fig. 3e*)* and Si-K-edge (Fig. 3f*)* thus suggesting the presence of the Si–O–Fe linkages. Which may be associated with the fifth coordination on the Fe-N_4 moiety in the RH-Fe-N catalyst. The quality of the fit with a reduced chi-square of 18.5 and an R-factor of 0.0086 and physical relevance of the paths as discussed above suggests the potential presence of interfacial bonding between the Fe species and the silica(amorphous SiO_2) matrix. These results lend support to the earlier hypothesis that SiO_2 not only acts as a structural support but also helps anchor Fe centers, potentially stabilizing Fe–N_4 active sites via a fifth coordination originating from Fe–O–Si linkages.

With the confirmed existence of a fifth coordination originating from oxygen ligand, the question of to what extent this linkage is contributing to the catalyst's stability was still prevalent. To address this ambiguity, comfort was sought from theoretical calculations using DFT models. Previous studies have demonstrated that the adsorption of O_2 molecules and the subsequent stretching of the O-O bond at the active sites play a critical role in the ORR mechanism [66]. DFT calculations in this work support this idea by examining the RH-Fe-N system with and without the presence of SiO_2. In the model without SiO_2, the central Fe ion experienced displacement from the Fe-N_4 ring plane (Nct-Fe = 0.331 Å), as shown in Fig. 4a due to the adsorption of O_2 and the elongation of the O-O bond. This displacement weakened the Fe-N_4 bond, increasing the

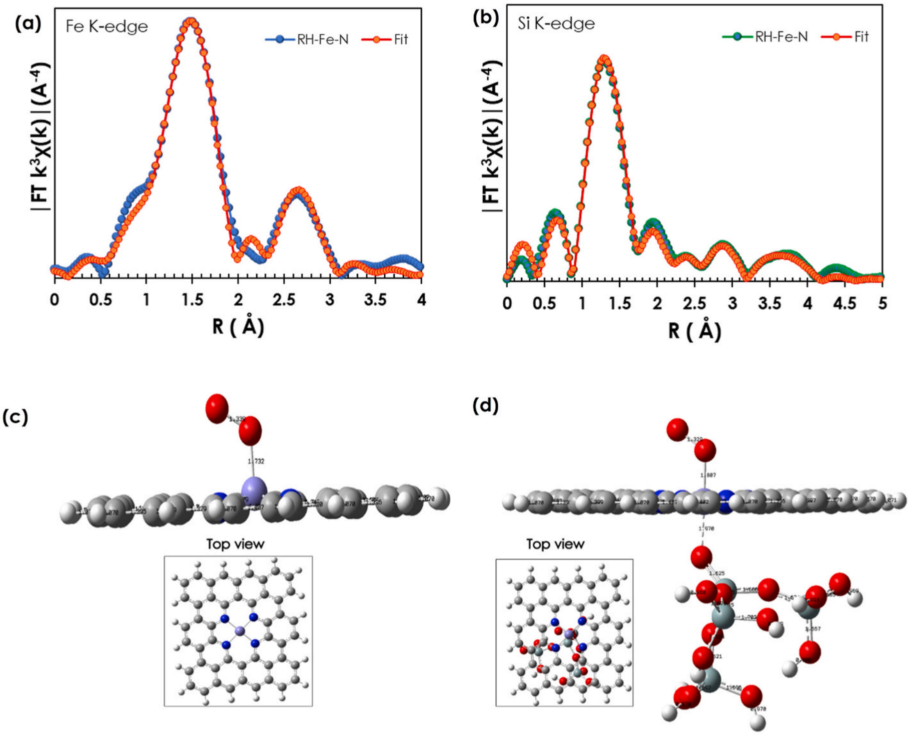

Fig. 4. **(a)** FT-EXAFS fitting curve in R space of RH-Fe-N at the Fe K-edge and (b) FT-EXAFS fitting curve in R space of RH-Fe-N at the Si K-edge. Density functional theory Optimized structure of RH-Fe-N. (c)Optimized structure of RH-Fe-N without amorphous SiO_2 and (d) corresponding optimized structure with amorphous SiO_2. Red spheres represent O_2 atoms, blue spheres represent nitrogen atoms, purple spheres represent Fe, grey spheres represent Si while dark grey spheres represent carbon. (For interpretation of the references to colour in this figure legend, the reader is referred to the Web version of this article.)

likelihood of Fe detaching from the catalytic site, which may lead to catalyst degradation. In contrast, when SiO_2 is included, the Fe ion remains firmly centered within the Fe-N_4 ring plane (Nct-Fe = 0.012 Å), as shown in Fig. 4b. This phenomenon hinted at the role SiO_2 played in stabilizing Fe-N_4 active sites, thus reducing the displacement of Fe and maintaining the integrity of the active site.

The impact of amorphous SiO_2 on the electronic structure of Fe was further analyzed by examining Mulliken charges on the Fe ion, with and without the SiO_2 ligand as shown in Figure.S15. In the model without SiO_2, the charge on Fe was 0.483, while with SiO_2, it increased to 0.727. This indicated that SiO_2 increased the electron density around the Fe ion, which enhanced O_2 adsorption, an important step in the ORR catalysis [67]. After O_2 adsorption, the Fe charge decreased to 0.689 in the presence of SiO_2, suggesting significant electron transfer from Fe to O. In the absence of SiO_2, the charge on Fe increased to 0.789, indicating weaker electron transfer. This behaviour supports the four-electron transfer mechanism, which is essential for efficient ORR catalysis [68]. In addition to improving the Fe-N_4 coordination, the presence of SiO_2 introduced an additional axial coordination between Fe and oxygen-based ligands originating from SiO_2, forming a fifth coordination site. This structural modification enhanced the adsorption and activation of O_2, leading to superior ORR activity compared to the traditional Fe-N_4 coordination found in commercial catalysts, such as phthalocyanine (FePc) catalysts [69]. The formation of this extra coordination site was key to improving both the catalytic activity and the stability of the RH-Fe-N catalyst as earlier exhibited.

Furthermore, the role of amorphous SiO_2 in enhancing catalyst durability was crucial. In the absence of SiO_2, the larger displacement of the Fe ion from the Fe-N_4 ring could increase the likelihood of Fe detaching from the macrocycle, leading to catalyst degradation and reduced long-term stability [43]. This was experimentally confirmed through a durability test comparing RH-Fe-N with commercial 40 wt% Pt/C catalysts, as shown in Fig. S7 for all pH media. These findings highlight that the superior durability of RH-Fe-N catalysts was not only due to the homogeneous dispersion of doped heteroatoms (Si, Fe, and N) in the carbon matrix but also the stabilizing effect of SiO_2 on the Fe-N_4 active sites. SiO_2 helped prevent the detachment of Fe from the active sites, preventing catalyst erosion, especially under low pH conditions. This stabilization promoted faster interfacial charge transfer, a key factor in maintaining high catalytic efficiency over time [59].

Therefore, the combination of homogeneous heteroatom doping and the stabilizing effect of SiO_2 in the RH-Fe-N catalyst significantly enhanced its durability, ensuring sustained high activity over extended periods. These properties are crucial for real-world energy applications, where long-lasting and reliable catalytic performance is essential. To corroborate the practical applicability of RH-Fe-N, a homemade aqueous Zn–air battery (ZAB) was assembled using an RH-Fe-N-CB loaded gas diffusion layer carbon paper as the cathode. As shown in Fig. S16a, RH-Fe-N-CB achieved a peak power density of approximately 160 $mWcm^{-2}$ outperforming the commercial Pt/C (40 wt%) benchmark, which attained around 120 $mWcm^{-2}$. This was consistent with an open circuit voltage of around 1.50 V against 1.40 V by Pt/C. This reflected a short-term stability test where RH-Fe-N-CB maintained a stable discharge voltage of over 10 min, slightly exceeding that of Pt/C, indicating good operational stability under constant load Fig. S16b.

The galvanostatic discharge profiles on the other hand at varying current densities Fig. S16c indicated that RH-Fe-N-CB consistently delivered higher voltages across all current steps. The voltage recovery upon returning to 5 $mAcm^{-2}$ confirmed an excellent reversibility and durability. In addition, a comparison of the key performance metrics for performance of the as-assembled ZABs among recently reported catalysts indicated that RH-Fe-N-CB had remarkable competitive activity and output in practical applications Table S3.

4. Conclusion

In summary, this work presents a sustainable and cost-effective Fe–N–C-based electrocatalyst (RH-Fe-N-CB) derived from rice husk, pyrite and urea, synthesized via a NaCl-templated carbonization strategy. This approach yielded a highly microporous carbon matrix that enhances mass transport and active site accessibility. The catalyst exhibited excellent ORR activity across a wide pH range, achieving half-wave potentials ($E_{1/2}$) of 0.84 V vs. RHE in alkaline and 0.71 V vs. RHE in both acidic and neutral media outperforming many state-of-the-art non-precious metal catalysts as summarized under Table S4,Table S5 and Table S6 for alkaline, near neutral and acidic respectively.

The superior performance is attributed to the formation of Fe–N_4 moieties and possible fifth Fe–O coordination, potentially facilitated by the self-doped amorphous SiO_2 from RH. This not only increased the number of active sites but also modified the carbon lattice to enhance the adsorption of N and Fe functional groups, further boosting catalytic activity and stability in not only alkaline environment but also in the harsh acidic environments hence underscoring its potential for energy applications like metal-air batteries. When evaluated in a zinc–air battery, RH-Fe-N-CB delivers a high open-circuit voltage of 1.50 V and a peak power density of 160 $mWcm^{-2}$, surpassing commercial 40 wt% Pt/C by almost 25 %. This work underscores the potential of biomass-derived electrocatalysts as viable, scalable alternatives to precious-metal-based systems for high-performance energy conversion devices.

CRediT authorship contribution statement

Edwin Osebe Nyangau: Writing – original draft, Visualization, Validation, Methodology, Investigation, Formal analysis, Data curation. **Hiroya Abe:** Writing – review & editing, Validation, Resources, Methodology, Formal analysis. **Kazutoshi Haga:** Resources, Methodology. **Chie Ooka:** Investigation. **Kenji Hayashida:** Writing – review & editing, Investigation, Formal analysis. **Naoka Nagamura:** Writing – review & editing, Validation. **Kotaro Takeyasu:** Writing – review & editing, Formal analysis, Data curation. **Masaru Watanabe:** Writing – review & editing, Resources. **Yuta Nakayasu:** Writing – review & editing, Visualization, Validation, Supervision, Resources, Project administration, Methodology, Funding acquisition, Conceptualization.

Data availability statement

The data that support the findings of this study are available from the corresponding author upon reasonable request.

Declaration of competing interest

The authors declare that they have no known competing financial interests or personal relationships that could have appeared to influence the work reported in this paper.

Acknowledgements

This work was supported by the Japan Society for the Promotion of Science (JSPS) KAKENHI [grant number 22K14533], the Environment Research and Technology Development Fund (JPMEERF20223C04 and JPMEERF20223R02) from the Environmental Restoration and Conservation Agency, Ministry of the Environment of Japan, and the Tohoku Initiative for Fostering Global Researchers for Interdisciplinary Sciences (TI-FRIS) under MEXT's Strategic Professional Development Program for Young Researchers. We also acknowledge the generous support from the FRIS CoRE, Tohoku University, a shared research facility.

Appendix A. Supplementary data

Supplementary data to this article can be found online at https://doi.

org/10.1016/j.jpowsour.2025.237784.

Data availability

Data will be made available on request.

References

[1] M. Kordi, N. Farrokhi, M.I. Pech-Canul, A. Ahmadikhah, Rice Sci. 31 (2024) 14–32, https://doi.org/10.1016/j.rsci.2023.08.005.

[2] H. Abe, Y. Nakayasu, K. Haga, M. Watanabe, Glob. Challenges. 7 (2023) 2300112, https://doi.org/10.1002/gch2.202300112.

[3] N. Shukla, D. Sahoo, N. Remya, J. Clean. Prod. 235 (2019) 1073–1079, https://doi.org/10.1016/j.jclepro.2019.07.042.

[4] H. Elbasiouny, B.A. Elbanna, E. Al-Najoli, A. Alsherief, S. Negm, E. Abou El-Nour, A. Nofal, S. Sharabash, Waste Manag. MENA Reg. (2019) 149–169, https://doi.org/10.1007/978-3-030-18350-9_8.

[5] A.A. Baba, K.I. Ayinla, F.A. Adekola, M.K. Ghosh, O.S. Ayanda, R.B. Bale, S. R. Pradhan, Int. J. Min. Eng. Miner. Process. 1 (2012) 1–16, https://doi.org/10.5923/j.mining.20120101.01.

[6] C.M. Oliveira, C.M. Machado, G.W. Duarte, M. Peterson, J. Clean. Prod. 139 (2016) 821–827, https://doi.org/10.1016/j.jclepro.2016.08.124.

[7] C. Owusu, S.B. Abreu, W. Skinner, J. Addai-Mensah, M. Zanin, Miner. Eng. 55 (2014) 87–95, https://doi.org/10.1016/j.mineng.2013.09.018.

[8] L.P. Ferreira, T.G. Müller, M. Cargnin, C.M. De Oliveira, M. Peterson, J. Environ. Chem. Eng. 9 (2021) 105759, https://doi.org/10.1016/j.jece.2021.105759.

[9] R. Liu, A.L. Wolfe, D.A. Dzombak, C.P. Horwitz, B.W. Stewart, R.C. Capo, Appl. Geochem. 23 (2008) 2724–2734, https://doi.org/10.1016/j.apgeochem.2008.06.005.

[10] P. Kaur, G. Verma, S.S. Sekhon, Prog. Mater. Sci. 102 (2019) 1–71, https://doi.org/10.1016/j.pmatsci.2018.12.002.

[11] Y. Liu, K. Sun, X. Cui, B. Li, J. Jiang, ACS Sustainable Chem. Eng. 8 (2020) 2981–2989, https://doi.org/10.1021/acssuschemeng.9b07621.

[12] L. Du, G. Zhang, X. Liu, A. Hassanpour, M. Dubois, A.C. Tavares, S. Sun, Carbon Energy 2 (2020) 561–581, https://doi.org/10.1002/cey2.73.

[13] O.A. Fakayode, B.A. Yusuf, C. Zhou, Y. Xu, Q. Ji, J. Xie, H. Ma, Energy Convers. Manage. 227 (2021) 113628, https://doi.org/10.1016/j.enconman.2020.113628.

[14] Y. Nakayasu, Y. Goto, Y. Katsuyama, T. Itoh, M. Watanabe, Carbon Trends 8 (2022) 100190, https://doi.org/10.1016/j.cartre.2022.100190.

[15] A. Dessalle, J. Quílez-Bermejo, V. Fierro, F. Xu, A. Celzard, Carbon 203 (2023) 237–260, https://doi.org/10.1016/j.carbon.2022.11.073.

[16] X. Ning, Y. Li, J. Ming, Q. Wang, H. Wang, Y. Cao, F. Peng, Y. Yang, H. Yu, Chem. Sci. 10 (2019) 1589–1596, https://doi.org/10.1039/C8SC04596H.

[17] S. Susanto, T. Nurtono, W. Widiyastuti, M.H. Yeh, H. Setyawan, ACS Omega 9 (2024) 13994–14004, https://doi.org/10.1021/acsomega.3c09297.

[18] Y. Goto, Y. Nakayasu, H. Abe, Y. Katsuyama, T. Itoh, M. Watanabe, Philos. Trans. R. Soc. A 379 (2021) 20200348, https://doi.org/10.1098/rsta.2020.0348.

[19] R. Jasinski, Nature 201 (1964) 1212–1213, https://doi.org/10.1038/2011212a0.

[20] Z. Chen, D. Higgins, A. Yu, L. Zhang, J. Zhang, Energy Environ. Sci. 4 (2011) 3167–3192, https://doi.org/10.1039/C0EE00558D.

[21] S. Kattel, P. Atanassov, B. Kiefer, Phys. Chem. Chem. Phys. 16 (2014) 13800–13806, https://doi.org/10.1039/C4CP01634C.

[22] Y. He, Q. Tan, L. Lu, J. Sokolowski, G. Wu, Electrochem. Energy Rev. 2 (2019) 231–251, https://doi.org/10.1007/s41918-019-00031-9.

[23] E.J. Biddinger, U.S. Ozkan, J. Phys. Chem. C 114 (2010) 15306–15314, https://doi.org/10.1021/jp104074t.

[24] T. Xing, Y. Zheng, L.H. Li, B.C. Cowie, D. Gunzelmann, S.Z. Qiao, S. Huang, Y. Chen, ACS Nano 8 (2014) 6856–6862, https://doi.org/10.1021/nn501506p.

[25] J. Wu, L. Ma, R.M. Yadav, Y. Yang, X. Zhang, R. Vajtai, J. Lou, P.M. Ajayan, ACS Appl. Mater. Interfaces 7 (2015) 14763–14769, https://doi.org/10.1021/acsami.5b02902.

[26] J.H. Zagal, M.T. Koper, Angew. Chem. Int. Ed. 55 (2016) 14510–14521, https://doi.org/10.1002/anie.201604311.

[27] J. Müller-Hülstede, H. Schmies, D. Schonvogel, Q. Meyer, Y. Nie, C. Zhao, P. Wagner, M. Wark, Int. J. Hydrogen Energy 50 (2024) 921–930, https://doi.org/10.1016/j.ijhydene.2023.09.190.

[28] A. Gabe, R. Ruiz-Rosas, C. González-Gaitán, E. Morallón, D. Cazorla-Amorós, J. Power Sources 412 (2019) 451–464, https://doi.org/10.1016/j.jpowsour.2018.11.075.

[29] D. Barrera, M. Florent, K. Sapag, T.J. Bandosz, ACS Appl. Energy Mater. 2 (2019) 7412–7424, https://doi.org/10.1021/acsaem.9b01427.

[30] A. Pedersen, K. Kumar, Y.P. Ku, V. Martin, L. Dubau, K.T. Santos, J. Barrio, V. Saveleva, P. Glatzel, V. Paidi, X. Li, Energy Environ. Sci. 17 (2024) 6323–6337, https://doi.org/10.26434/chemrxiv-2024-7p3cm.

[31] Q. Ma, H. Jin, J. Zhu, Z. Li, H. Xu, B. Liu, Z. Zhang, J. Ma, S. Mu, Adv. Sci. 8 (2021) 2102209, https://doi.org/10.1002/advs.202102209.

[32] Y. Lian, J. Xu, W. Zhou, Y. Lin, J. Bai, Molecules 29 (2024) 771, https://doi.org/10.3390/molecules29040771.

[33] N.H. Junaidi, W.Y. Wong, K.S. Loh, S. Rahman, T.F. Choo, B. Wu, J. Alloys Compd. 968 (2023) 171898, https://doi.org/10.1016/j.jallcom.2023.171898.

[34] Y.C. Lin, P.Y. Teng, C.H. Yeh, M. Koshino, P.W. Chiu, K. Suenaga, Nano Lett. 15 (2015) 7408–7413, https://doi.org/10.1021/acs.nanolett.5b02831.

[35] H. Abe, Y. Hirai, S. Ikeda, Y. Matsuo, H. Matsuyama, J. Nakamura, T. Matsue, H. Yabu, NPG Asia Mater. 11 (2019) 57, https://doi.org/10.1038/s41427-019-0154-6.

[36] J. Quílez-Bermejo, S. Pérez-Rodríguez, R. Canevesi, D. Torres, E. Morallón, D. Cazorla-Amorós, A. Celzard, V. Fierro, Carbon 196 (2022) 708–717, https://doi.org/10.1016/j.carbon.2022.05.032.

[37] I. Ayyubov, E. Tálas, C. Berghian-Grosan, L. Románszki, I. Borbáth, Z. Pászti, Á. Szegedi, J. Mihály, A. Vulcu, A. Tompos, React. Kinet. Mech. Catal. 136 (2023) 125–147, https://doi.org/10.1007/s11144-022-02331-6.

[38] F. Kong, X. Cui, Y. Huang, H. Yao, Y. Chen, H. Tian, G. Meng, C. Chen, Z. Chang, J. Shi, Angew. Chem. Int. Ed. 61 (2022) e202116290, https://doi.org/10.1002/anie.202116290.

[39] G. Li, K. Sheng, Y. Lei, J. Yang, Y. Chen, X. Guo, G. Chen, B. Chang, T. Wu, X. Wang, Chem. Eng. J. 451 (2023) 138823, https://doi.org/10.1016/j.cej.2022.138823.

[40] J. Liu, L. Wei, H. Wang, G. Lan, H. Yang, J. Shen, Int. J. Hydrogen Energy 45 (2020) 29308–29321, https://doi.org/10.1016/j.ijhydene.2020.07.216.

[41] H. Wang, W. Zhang, P. Bai, L. Xu, Ultrason. Sonochem. 65 (2020) 105048, https://doi.org/10.1016/j.ultsonch.2020.105048.

[42] L. Yu, C. Yang, W. Zhang, W. Liu, H. Wang, J. Qi, L. Xu, J. Colloid Interface Sci. 575 (2020) 406–415, https://doi.org/10.1016/j.jcis.2020.05.012.

[43] E.F. Holby, G. Wang, P. Zelenay, ACS Catal. 10 (2020) 14527–14539, https://doi.org/10.1021/acscatal.0c02856.

[44] Z. Huang, F. Li, Y. Liu, S. Chen, Z. Wei, Q. Tang, Chem. Sci. 15 (2024) 1132–1142, https://doi.org/10.1039/D3SC05378D.

[45] M. J. Frisch. Gaussian 09, Revision D. 01/Gaussian..

[46] K. Kim, K.D. Jordan, J. Phys. Chem. 98 (1994) 10089–10094, https://doi.org/10.1021/j100091a024.

[47] H. Matsuyama, A. Akaishi, J. Nakamura, ACS Omega 4 (2019) 3832–3838, https://doi.org/10.1021/acsomega.9b00015.

[48] E.D. Ingall, Y. Feng, A.F. Longo, B. Lai, R.U. Shelley, W.M. Landing, P.L. Morton, A. Nenes, N. Mihalopoulos, K. Violaki, Y. Gao, Atmosphere 9 (2018) 201. https://www.mdpi.com/2073-4433/9/5/201.

[49] F. Wang, Q. Li, Z. Xiao, B. Jiang, J. Ren, Z. Jin, X. Tang, Y. Chen, X. Li, J. Colloid Interface Sci. 606 (2022) 1014–1023, https://doi.org/10.1016/j.jcis.2021.08.117.

[50] W. Ding, L. Li, K. Xiong, Y. Wang, W. Li, Y. Nie, S. Chen, X. Qi, Z. Wei, J. Am. Chem. Soc. 137 (2015) 5414–5420, https://doi.org/10.1021/jacs.5b00292.

[51] Y. Nie, J. Deng, W. Jin, W. Guo, G. Wu, M. Deng, J. Zhou, R. Yang, S. Zhang, Z. Wei, J. Alloys Compd. 884 (2021) 161063, https://doi.org/10.1016/j.jallcom.2021.161063.

[52] L. Diao, W. Zhou, B. Zhang, C. Shi, Z. Miao, J. Zhou, C. He, J. Colloid Interface Sci. 645 (2023) 329–337, https://doi.org/10.1016/j.jcis.2023.04.080.

[53] P. Zhang, H.C. Chen, H. Zhu, K. Chen, T. Li, Y. Zhao, J. Li, R. Hu, S. Huang, W. Zhu, Y. Liu, Nat. Commun. 15 (2024) 2062, https://doi.org/10.1038/s41467-024-46389-3.

[54] D.W. Kim, O.L. Li, N. Saito, Phys. Chem. Chem. Phys. 17 (2015) 407–413, https://doi.org/10.1039/C4CP03868A.

[55] J. Yan, T. Gu, R. Shi, X. Chen, M.H. Rümmeli, R. Yang, J. Mater. Chem. A 11 (2023) 16180–16189, https://doi.org/10.1039/D3TA02712K.

[56] A.G. Volkov, S. Paula, D.W. Deamer, Bioelectrochem. Bioenerg. 42 (1997) 153–160, https://doi.org/10.1016/S0302-4598(96)05097-0.

[57] M.Y. Kiriukhin, K.D. Collins, Biophys. Chem. 99 (2002) 155–168, https://doi.org/10.1016/S0301-4622(02)00153-9.

[58] T.G. Vo, J. Gao, Y. Liu, Adv. Funct. Mater. (2024) 2314282., https://doi.org/10.1002/adfm.202314282.

[59] S. Onajah, R. Sarkar, M.S. Islam, M. Lalley, K. Khan, M. Demir, H.N. Abdelhamid, A.A. Farghaly, The Chem. Record 24 (2024) e202300234, https://doi.org/10.1002/tcr.202300234.

[60] S.K. Singh, K. Takeyasu, K. Homma, S. Ito, T. Morinaga, Y. Endo, M. Furukawa, T. Mori, H. Ogasawara, J. Nakamura, Angew. Chem. 134 (2022) e202212506, https://doi.org/10.1002/ange.202212506.

[61] E.O. Nyangau, H. Abe, Y. Nakayasu, M. Umetsu, M. Watanabe, C. Tada, Bioresource Technol. Rep 23 (2023) 101565, https://doi.org/10.1016/j.biteb.2023.101565.

[62] X. Wan, Q. Liu, J. Liu, S. Liu, X. Liu, L. Zheng, J. Shang, R. Yu, J. Shui, Nat. Commun. 13 (2022) 2963, https://doi.org/10.1038/s41467-022-30702-z.

[63] G. Calas, G.E. Brown, G.A. Waychunas, J. Petiau, Phys. Chem. Miner. 15 (1987) 19–29, https://doi.org/10.1007/BF00307604.

[64] M.W. Chung, G. Chon, H. Kim, F. Jaouen, C.H. Choi, Chemelectrochem 5 (2018) 1880–1885, https://doi.org/10.1002/celc.201800067.

[65] B. Ravel, M. Newville, Synchrotron Radiation 12 (4) (2005) 537–541.

[66] R. Cao, R. Thapa, H. Kim, X. Xu, M. Gyu Kim, Q. Li, N. Park, M. Liu, J. Cho, Nat. Commun. 4 (2013) 2076, https://doi.org/10.1038/ncomms3076.

[67] S. Yang, C. Zhao, R. Qu, Y. Cheng, H. Liu, X. Huang, RSC Adv. 11 (2021) 3174–3182, https://doi.org/10.1039/D0RA08652E.

[68] K. Liu, J. Fu, Y. Lin, T. Luo, G. Ni, H. Li, Z. Lin, M. Liu, Nat. Commun. 13 (2022) 2075, https://doi.org/10.1038/s41467-022-29797-1.

[69] K. Chen, K. Liu, P. An, H. Li, Y. Lin, J. Hu, C. Jia, J. Fu, H. Li, H. Liu, Z. Lin, Nat. Commun. 11 (2020) 4173, https://doi.org/10.1038/s41467-020-18062-y.